



# Production cross sections from $^{82}\text{Se}$ fragmentation as indications of shell effects in neutron-rich isotopes close to the drip-line

O. B. Tarasov,<sup>1,\*</sup> M. Portillo,<sup>2</sup> D. J. Morrissey,<sup>1,3</sup> A. M. Amthor,<sup>2</sup> L. Bandura,<sup>2</sup> T. Baumann,<sup>1</sup> D. Bazin,<sup>1</sup> J. S. Berryman,<sup>1</sup> B. A. Brown,<sup>1,4</sup> G. Chubarian,<sup>5</sup> N. Fukuda,<sup>6</sup> A. Gade,<sup>1,4</sup> T. N. Ginter,<sup>1</sup> M. Hausmann,<sup>2</sup> N. Inabe,<sup>6</sup> T. Kubo,<sup>6</sup> J. Pereira,<sup>1</sup> B. M. Sherrill,<sup>1,4</sup> A. Stolz,<sup>1</sup> C. Sumithrarachichi,<sup>1</sup> M. Thoennessen,<sup>1,4</sup> and D. Weisshaar<sup>1</sup>

<sup>1</sup>*National Superconducting Cyclotron Laboratory, Michigan State University, East Lansing, Michigan 48824, USA*

<sup>2</sup>*Facility for Rare Isotope Beams, Michigan State University, East Lansing, Michigan 48824, USA*

<sup>3</sup>*Department of Chemistry, Michigan State University, East Lansing, Michigan 48824, USA*

<sup>4</sup>*Department of Physics and Astronomy, Michigan State University, East Lansing, Michigan 48824, USA*

<sup>5</sup>*Cyclotron Institute, Texas A&M University, College Station, Texas 77843, USA*

<sup>6</sup>*RIKEN Nishina Center, RIKEN, Wako-shi, Saitama 351-0198, Japan*

(Received 11 February 2013; published 20 May 2013)

Production cross sections for neutron-rich nuclei from the fragmentation of a  $^{82}\text{Se}$  beam at 139 MeV/u were measured. The longitudinal momentum distributions of 126 neutron-rich isotopes of elements  $11 \leq Z \leq 32$  were scanned using an experimental approach of varying the target thickness. Production cross sections with beryllium and tungsten targets were determined for a large number of nuclei including several isotopes first observed in this work. These are the most neutron-rich nuclides of the elements  $22 \leq Z \leq 25$  ( $^{64}\text{Ti}$ ,  $^{67}\text{V}$ ,  $^{69}\text{Cr}$ , and  $^{72}\text{Mn}$ ). One event was registered consistent with  $^{70}\text{Cr}$  and another one with  $^{75}\text{Fe}$ . The production cross sections are correlated with  $Q_g$  systematics to reveal trends in the data. The results presented here confirm our previous results from a similar measurement using a  $^{76}\text{Ge}$  beam and can be explained with a shell model that predicts a subshell closure at  $N = 34$  around  $Z = 20$ . This is demonstrated by systematic trends and calculations with the abrasion-ablation model that are sensitive to separation energies.

DOI: [10.1103/PhysRevC.87.054612](https://doi.org/10.1103/PhysRevC.87.054612)

PACS number(s): 25.70.Mn, 27.40.+z, 27.50.+e, 21.60.Cs

## I. INTRODUCTION

### A. Discovery of new nuclei

The discovery of new nuclei in the proximity of the neutron drip-line provides a stringent test for nuclear mass models and hence for the understanding of both the nuclear force and the creation of elements. Another important aspect of such measurements is that once neutron-rich nuclei are observed and their cross sections for formation are understood, investigations to study the nuclei themselves, such as with decay spectroscopy, can be planned. Therefore, obtaining production rates for the most exotic nuclei continues to be an important part of the experimental program at existing and future rare-isotope facilities.

A number of production mechanisms have been used to produce neutron-rich isotopes for  $20 \leq Z \leq 28$  [1] but, in the last few years, two reaction mechanisms were the most effective at producing nuclei in this region:

- (i) projectile fragmentation—an experiment with a  $^{76}\text{Ge}$  (132 MeV/u) beam produced 15 new isotopes of  $17 \leq Z \leq 25$  [2],
- (ii) in-flight fission with light targets (abrasion-fission)—an experiment with a  $^{238}\text{U}$  beam [3] produced a large number of isotopes of  $25 \leq Z \leq 48$  using a Be target and several new isotopes with  $46 \leq Z \leq 56$  by Coulomb fission on a heavy target.

Progress in the production of neutron-rich isotopes was made possible by the increase of primary beam intensities, new beam development at the National Superconducting Cyclotron Laboratory (NSCL) at Michigan State University, and advances in experimental techniques [4]. Indeed, recent measurements at the NSCL [1,4–6] have demonstrated that the fragmentation of  $^{48}\text{Ca}$  and  $^{76}\text{Ge}$  beams can be used to produce new isotopes in the proximity of the neutron drip-line. Continuing this work, we report here the next step with a newly developed  $^{82}\text{Se}$  beam towards the fundamental goal of defining the absolute mass limit for chemical elements in the region of calcium. In the present measurement, four neutron-rich isotopes with  $42 \leq N \leq 47$  were identified for the first time (see Fig. 1), one event was registered consistent with  $^{70}\text{Cr}_{46}$ , and another one was registered consistent with  $^{75}\text{Fe}_{49}$ .

### B. Evidence for global structure changes

One of the first indications of significant changes in the structure of neutron-rich nuclei was the discovery of enhanced nuclear binding of heavy sodium isotopes [8]. This is now understood to result from significant contributions of  $fp$  shell intruder orbitals to the ground-state configurations of these isotopes [9,10]. Low-lying  $2^+$  states and quadrupole collectivity have been reported in neutron-rich even-even Ne and Mg isotopes around  $N = 20$  (see, for example, Refs. [11–15]). This region around  $^{31}\text{Na}$ , where the neutron  $fp$  shell contributes significantly to the ground-state structure, is now known as the “island of inversion.” Similarly, there is mounting evidence for an onset of deformation around neutron number  $N = 40$  in Fe and Cr nuclei. In even-even Fe and Cr nuclei, for example,

\*On leave from Flerov Laboratory of Nuclear Reactions, JINR, 141980 Dubna, Moscow Region, Russian Federation; tarasov@nscl.msu.edu

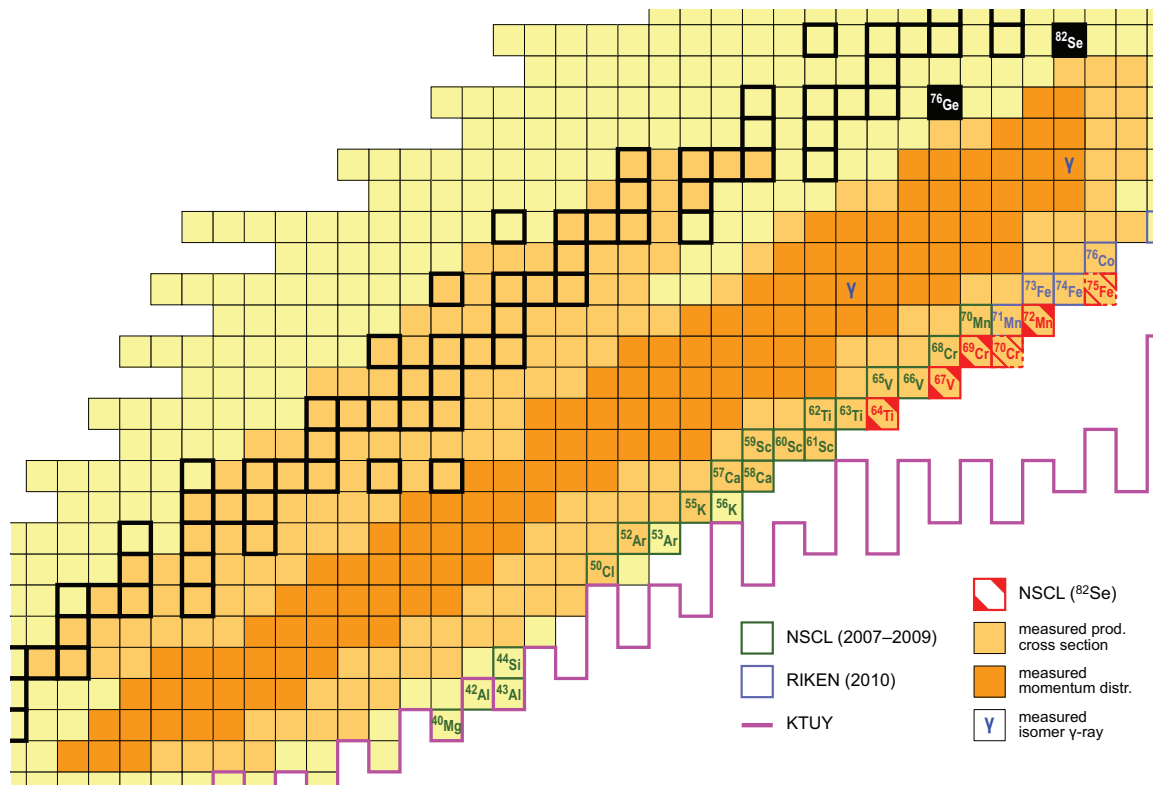


FIG. 1. (Color online) The region of the nuclear chart investigated in the present work. The solid line shows the limit of bound nuclei from the KTUY mass model [7]. The new isotopes observed for the first time in the present work are marked by red squares.

this evidence is based on the energies of low-lying states [16–20], transition strengths [21], deformation length [19], and higher-spin level schemes [22]. Neutron  $g_{9/2}$  and  $d_{5/2}$  configurations from above the  $N = 40$  shell gap are proposed to descend and dominate the low-lying configurations similar to those in the  $N = 20$  island of inversion [23,24].

Recently, it was shown that the  $\beta$ -decay half-lives of the neutron-rich Ca isotopes [25] compare favorably with the results of shell-model calculations performed in the full  $pf$  model space using the GXPF1 effective interaction [26]. The systematic trend of these half-lives is consistent with the presence of a subshell gap at  $N = 32$  as predicted by this interaction and confirmed by a variety of experiments. This interaction also predicts an increase of the excitation energy of the first excited state  $E_x(2_1^+)$  at  $^{54}\text{Ca}$  relative to that obtained with the KB3G [27] interaction, suggesting the appearance of the  $N = 34$  shell gap in Ca isotopes. Both interactions predict similar structures for light stable nuclei, but give rather different predictions for several cases of neutron-rich nuclei.

Recent measurements at RIKEN of the  $E_x(2_1^+)$  in  $^{54}\text{Ca}$  [28] found that the experimental value is 0.5 MeV smaller than the GXPF1B prediction, where the GXPF1B [29] Hamiltonian was created from the GXPF1A Hamiltonian by changing five  $T = 1$  matrix elements and the single-particle energies that involved  $1p_{1/2}$ . A similar trend had already been pointed out by Mantica *et al.* [25] where they deduce that the effective energy gap between the adjacent neutron single-particle orbitals  $f_{5/2}$  and  $p_{1/2}$  is overestimated by the GXPF1 and GXPF1A effective interactions. Based on this, the GXPF1B interaction

has been modified to correct this 0.5-MeV shift and is referred to as GXPF1B5 here.

Other evidence supports the modified form of the GXPF1B interaction. The original GXPF1B interaction predicts a  $1n$ -unbound  $^{56}\text{K}$  ( $S_{1n} = -0.03$  MeV); however, this isotope was shown to be bound by observation in our previous experiment with the  $^{76}\text{Ge}$  beam. The shift in the interaction makes the isotopes with valence neutrons in the  $f_{5/2}$  orbital around  $Z = 20$  more bound, such that the modified interaction GXPF1B5 predicts a bound  $^{56}\text{K}$  with  $S_{1n} = 0.41$  MeV.

In our previous cross-section measurements in the region around  $^{62}\text{Ti}$  ( $^{76}\text{Ge}$  primary beam) [2] we observed a systematic variation of the production cross sections that might point to nuclear structure effects, such as an onset of collectivity, that are not included in global mass models that were used to construct the basis of the systematics. The present work, because it is based on isotope production from a different primary beam, covering the same region of the nuclear chart, provides an independent check of this interpretation.

## II. EXPERIMENT

### A. Setup

A newly developed 139 MeV/u  $^{82}\text{Se}$  beam with an intensity of 35 pA, accelerated by the coupled cyclotrons at the NSCL, was fragmented in a series of beryllium targets and a tungsten target, each placed at the object position of the A1900 fragment separator [30]. In this work we used a configuration identical to

TABLE I. Experimental settings.

Data set	Fragment of interest	Magnetic rigidity, $B\rho$ (Tm)					Target (mg/cm <sup>2</sup> )	Stripper (mg/cm <sup>2</sup> )	Wedge (mg/cm <sup>2</sup> )	$\Delta p/p$ (%)	Time (h)	Beam particles	Goal
		$D_1D_2$	$D_3D_4$	$D_5D_6D_7$	$D_8D_9$	$D_{10}D_{11}$							
1	$^{67}\text{Fe}$	4.3209	4.3209	4.3065	4.2919	4.2867	Be 9.7	–	–	0.1	1.13	3.76e12	
2							Be 68	–	–	0.1	1.01	3.06e12	
3							Be 138	–	–	0.1	0.69	4.32e13	Momentum distribution study
4							Be 230	–	–	0.1	1.17	2.00e14	
5							Be 314	–	–	0.2	1.03	1.05e14	
6							Be 413	–	–	0.2	1.45	2.60e14	
7							Be 513	–	–	0.2	1.60	4.13e14	
8	$^{67}\text{Fe}$	4.3412	4.3209	4.3065	4.2919	4.2867	Be 190	–	20	0.2	1.99	1.14e15	Isomer production
9	$^{78}\text{Zn}$	4.3505	4.3267	4.3099	4.2928	4.2867	Be 190	–	20	0.2	2.00	1.57e15	
10	$^{74}\text{Fe}$	4.3538	4.3289	4.3111	4.2931	4.2867	Be 557	–	20	5	37.4	3.22e16	Production of new isotopes
11	$^{75}\text{Fe}$	4.3560	4.3301	4.3118	4.2933	4.2867	W 750	Be 17.3	20	5	3.86	3.66e15	
12	$^{68}\text{V}$	4.3515	4.3274	4.3103	4.2929	4.2867	Be 695	–	20	5	42.6	3.77e16	
13	$^{60}\text{Ca}$	4.3451	4.3233	4.3079	4.2922	4.2867	Be 849	–	20	5	16.1	1.49e16	Stable Ca isotopes
14	$^{60}\text{Ca}$	4.3451	4.3233	4.3079	4.2922	4.2867	Be 695	–	20	5	14.8	1.18e16	
15	$^{45}\text{Ca}$	3.6331	3.6177	3.6055	3.5932	3.5888	Be 190	–	20	0.1	0.92	2.86e11	Stable Ca isotopes
16	$^{48}\text{Ca}$	3.6396	3.6219	3.6080	3.5939	3.5888	Be 190	–	20	0.1	1.55	2.50e11	

that of our previous experiment with a  $^{76}\text{Ge}$  beam [1], where the combination of the A1900 fragment separator with the S800 analysis beam line [31] formed a two-stage separator system, which allowed a high degree of rejection of unwanted reaction products. At the end of the S800 analysis beam line, the particles of interest were stopped in a telescope of eight silicon PIN diodes ( $50 \times 50 \text{ mm}^2$  each) with a total thickness of 8.0 mm. A 50-mm-thick plastic scintillator positioned behind the Si telescope served as a veto detector against reactions in the Si telescope and provided a measurement of the residual energy of lighter ions that were not stopped in the Si telescope. A position-sensitive parallel plate avalanche counter (PPAC) was located in front of the Si telescope. All experimental details and a sketch of the experimental setup can be found in Ref. [1]. In this paper, we describe the details of our experimental approach and discuss the results.

### B. Experimental runs

The present experiment consisted of four segments that are summarized in Table I. Except for the last segment, the present experimental program is similar to the previous  $^{76}\text{Ge}$  experiment [1]. During all runs, the magnetic rigidity of the last two dipoles of the analysis line was kept constant at a value of 4.2867 Tm while the production target thickness was varied to map the fragment momentum distributions. This approach greatly simplifies the particle identification during the scans of the parallel momentum distributions.

The momentum acceptance of the A1900 fragment separator was restricted to  $\Delta p/p = 0.1\%$  (first four runs with thin targets) and to  $\Delta p/p = 0.2\%$  (other targets) for the measurement of differential momentum distributions in the first part of the experiment. The use of different beryllium target thicknesses (9.7, 68, 138, 230, 314, 413, and 513 mg/cm<sup>2</sup>) allowed coverage of the fragment momentum distributions

necessary to extract production cross sections and also resulted in more isotopes in the particle identification spectrum.

For the second part of the experiment, a Kapton wedge with a thickness of 20.0 mg/cm<sup>2</sup> was used at the dispersive image of the A1900 with a 10-mm aperture in the focal plane to reject less exotic fragments while the separator was set for  $^{67}\text{Fe}$  and  $^{78}\text{Zn}$  ions. The goal of this setting was to confirm the particle identification by isomer tagging as described in Ref. [32] with  $^{67m}\text{Fe}$  ( $E_\gamma = 367 \text{ keV}$ ,  $T_{1/2} = 43 \mu\text{s}$ ) and  $^{78m}\text{Zn}$  ( $E_\gamma = 730, 890, \text{ and } 908 \text{ keV}$ ,  $T_{1/2} = 0.32 \mu\text{s}$ ).

In the third part of the experiment, dedicated to the search for new isotopes, five settings were used to cover the most neutron-rich isotopes with  $20 \leq Z \leq 27$ , as it was impossible to find a single target thickness and magnetic rigidity to observe all of the fragments of interest. Each setting was characterized by a fragment for which the separator was optimized. A search for the most exotic nuclei in each setting was carried out with Be and W targets. The settings were centered on  $^{60}\text{Ca}$ ,  $^{68}\text{V}$ , and  $^{74,75}\text{Fe}$  respectively, based on LISE<sup>++</sup> [33] calculations using the parametrizations of the momentum distributions obtained in the first part of the experiment (see Sec. IV A). The momentum acceptance of the A1900 was set to the maximum of  $\Delta p/p = 5.0\%$  for these production runs. It should be noted that the momentum acceptance of the S800 beamline is about 4% according to LISE<sup>++</sup> Monte Carlo simulations using a new extended configuration with fifth-order optics. This calculated acceptance has been used for the cross-section analysis using the method described below.

The fourth part of the experiment was devoted to two short runs measuring the yields of more stable isotopes by centering on  $^{45,48}\text{Ca}$ .

### III. ANALYSIS OF EXPERIMENTAL DATA

The result of our approach of keeping the last dipoles' magnetic rigidities constant while varying the target thickness—as

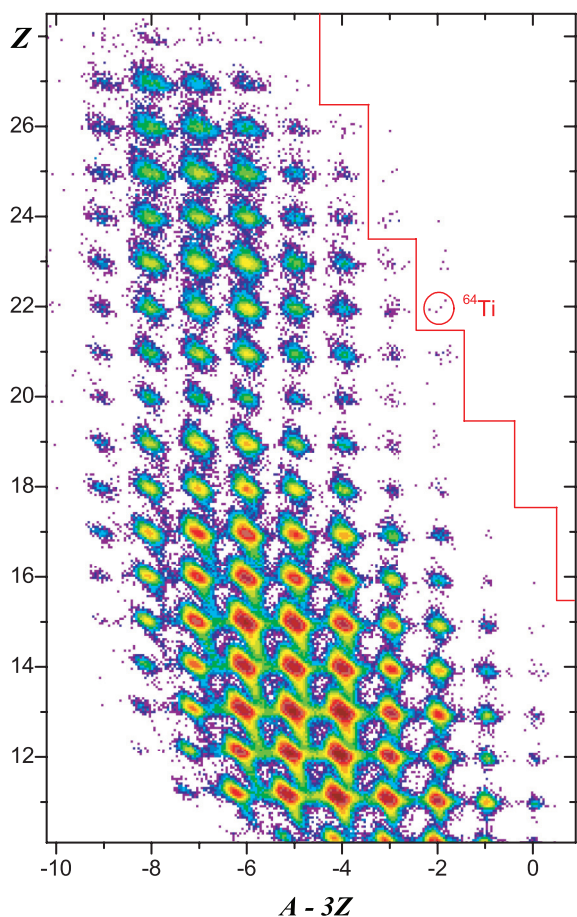


FIG. 2. (Color online) Particle identification plot showing the measured atomic number  $Z$  versus the calculated function  $A - 3Z$  for the nuclei observed in production runs of this work. See text for details. The limit of previously observed nuclei is shown by the solid red line, and the location of  $^{64}\text{Ti}$  is marked.

was done in the previous experiment—can be seen in Fig. 2, which shows the total distribution of fully stripped reaction products observed in the production runs of this work. The range of fragments is shown as a function of the measured atomic number  $Z$  versus the quantity  $A - 3Z$  deduced from measured values, where  $A$  is the mass number. The identification of the individual isotopes in Fig. 2 was confirmed via isomer tagging using the known isomeric decays in  $^{67}\text{Fe}$  and  $^{78}\text{Zn}$ . The standard deviations of ionic charge ( $q$ ) and elemental ( $Z$ ) spectra were found to be similar to those in the previous experiment; therefore the probabilities of one event being misidentified as a neighboring charge state or element are the same as before [1]. The details of the calculation of the particle identification are given in the appendix to the previous work [1].

The mass spectra for the isotopic chains from scandium to iron measured during the production runs are shown in Fig. 3. Only nuclei that stopped in the Si telescope are included in this analysis. The observed fragments include several new isotopes that are the most neutron-rich nuclides yet observed of elements  $22 \leq Z \leq 25$  ( $^{64}\text{Ti}$ ,  $^{67}\text{V}$ ,  $^{69}\text{Cr}$ , and  $^{72}\text{Mn}$ ). One event was found to be consistent with  $^{70}\text{Cr}$ , and another one

was found to be consistent with  $^{75}\text{Fe}$ . The new neutron-rich nuclei observed in this work lie to the right of the solid line in Fig. 2 and to the right of the vertical dashed lines in Fig. 3.

## IV. RESULTS AND DISCUSSION

### A. Parallel momentum distributions

The prediction of the momentum distributions of residues is important when searching for new isotopes in order to set the fragment separator at the maximum production rate. Also, the accurate prediction of the momentum distributions allows for a precise estimate of the transmission and efficient rejection of strong contaminants. In this experiment the “target scanning” approach [34], developed in the previous experiment, was used to obtain parameters for the neutron-rich isotope momentum distribution models such as those in Refs. [35,36]. This method is particularly well suited to survey neutron-rich nuclei because the less exotic nuclei are produced with the highest yields and their momentum distributions can be readily measured with thin targets.

The data analysis of this approach has been improved, and a detailed description is in preparation [37]. Important improvements include the following: first, the most probable velocity for a fragment is not that at the center of the target when the yield is sharply rising or falling with momentum, and second, asymmetric Gaussian distributions have been used with asymmetry coefficients taken from the convolution model [38] implemented in the LISE<sup>++</sup> code [33]. Note that, at the bombarding energy used in these experiments, the shape of the fragment momentum distribution is asymmetric with a low-energy exponential tail stemming from dissipative processes [38].

Seven targets were used to measure the momentum distributions (see Table I). The yield of one example fragment,  $^{66}\text{Fe}$ , is shown in Fig. 4 as a function of the ratio of fragment and beam velocities. This figure illustrates the impact of the new data analysis where the most probable values taken are shown by the circles and the average values by the diamonds. Momentum distributions for 126 isotopes were derived (indicated by the colored boxes in Fig. 1) and integrated to deduce the production cross sections.

A survey of all of the fitted results showed that fragments in the heavy mass region were produced similar to our previous measurements [34] with significantly higher velocities than the momentum distribution models [36,39] predict. The difference is most likely due to the fact that the models were developed for fragments close to stability, where the energy required to remove each nucleon was set to 8 MeV, while the actual nucleon binding energy for the neutron-rich isotopes under investigation is lower. An analysis with asymmetric distributions to reproduce the mean velocity of fragments has shown that the neutron-rich separation energy parameter in the model [36] for the nuclei observed in the present work in the region  $A_P/2 \leq A_F \leq A_P$  can be represented by a linear decrease with the number of removed nucleons:

$$E_S = 8 - 9.2\Delta A/A_P, \quad (1)$$

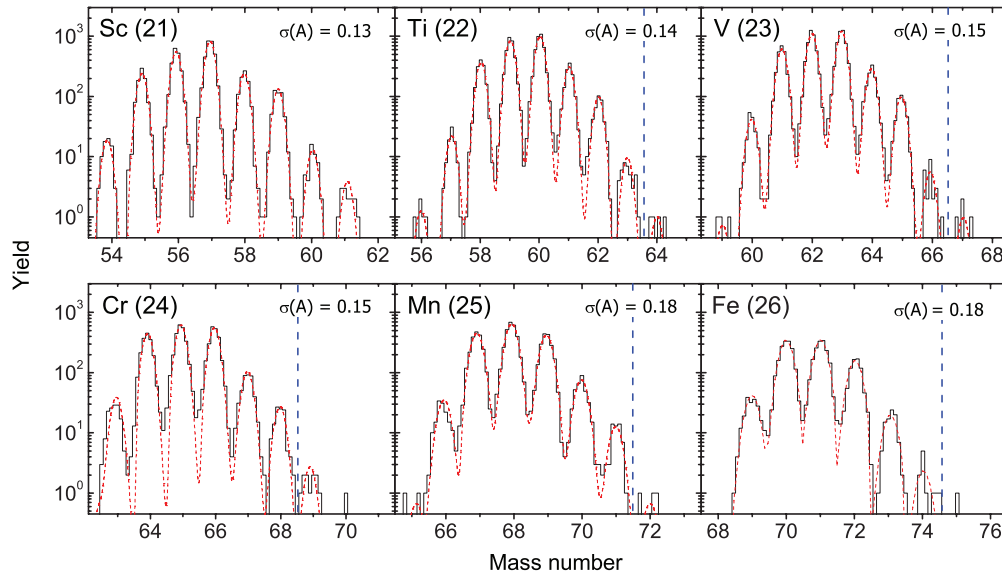


FIG. 3. (Color online) Mass spectra of the elements  $21 \leq Z \leq 26$  that were stopped in the Si telescope during the production runs. The limits of previously observed nuclei are shown by the vertical dashed lines. Standard deviations produced with the Gaussian function at constant width (dashed curves) are given in the panel figures for each element.

where  $\Delta A = A_P - A_F$ ,  $A_P$  is the projectile mass number, and  $A_F$  is the fragment mass number. In the fourth part of the experiment, where stable isotopes were measured (see Table I), no deviations from the default parameters of the model for the velocities were observed.

The width obtained for each fragment's parallel momentum distribution is presented in Fig. 5 for fragments produced from the interaction of  $^{82}\text{Se}$  (139 MeV/u) with  $^9\text{Be}$  targets. The pre-

dictions with best fits of reduced widths  $\sigma_0(G) = 87$  MeV/c for the Goldhaber model [35] and  $\sigma_0(M) = 75$  MeV/c for the Morrissey model [36] are presented in this figure.

## B. Production cross sections

The inclusive production cross sections for the observed fragments were calculated by correcting the measured yields for the finite momentum and angular acceptances of the

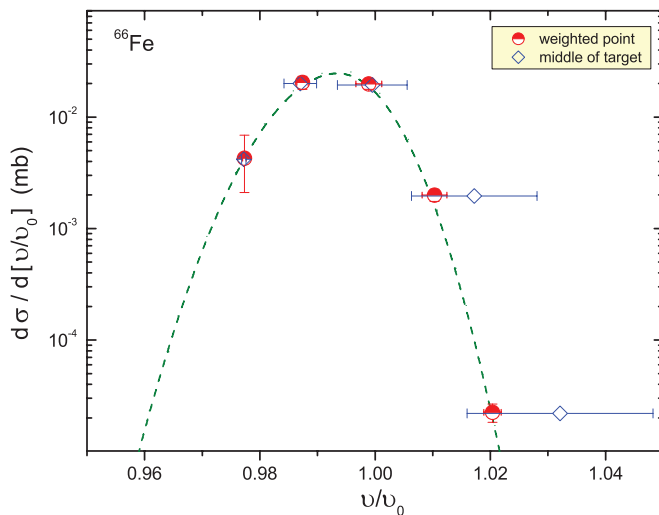


FIG. 4. (Color online) Differential cross sections of  $^{66}\text{Fe}$  fragments obtained by varying the target thickness with the analysis line set at one fixed magnetic rigidity. The dashed line represents the fitted asymmetric Gaussian function. Blue horizontal errors with diamonds in the center correspond to the velocity difference caused by production at the beginning or the end of target, whereas the red circles show the position of the most probable velocity based on the momentum distribution parametrization.

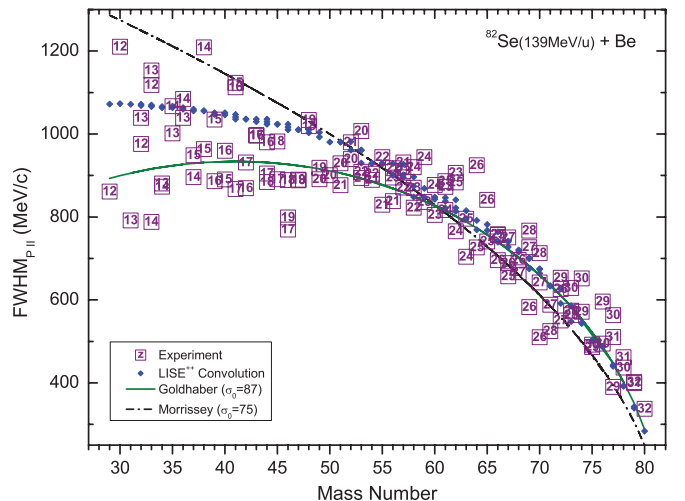


FIG. 5. (Color online) Widths of the parallel momentum component as a function of the mass number of fragments produced in the reaction  $^{82}\text{Se}$  beams with beryllium targets. Small diamonds denote calculations by the convolution model [38] with default settings for separation energy ( $E_s$ ) option #1 in LISE $^{++}$ . Solid green and dot-dashed black lines represent the best fit to the data for the Goldhaber [35] and Morrissey [36] models, respectively.

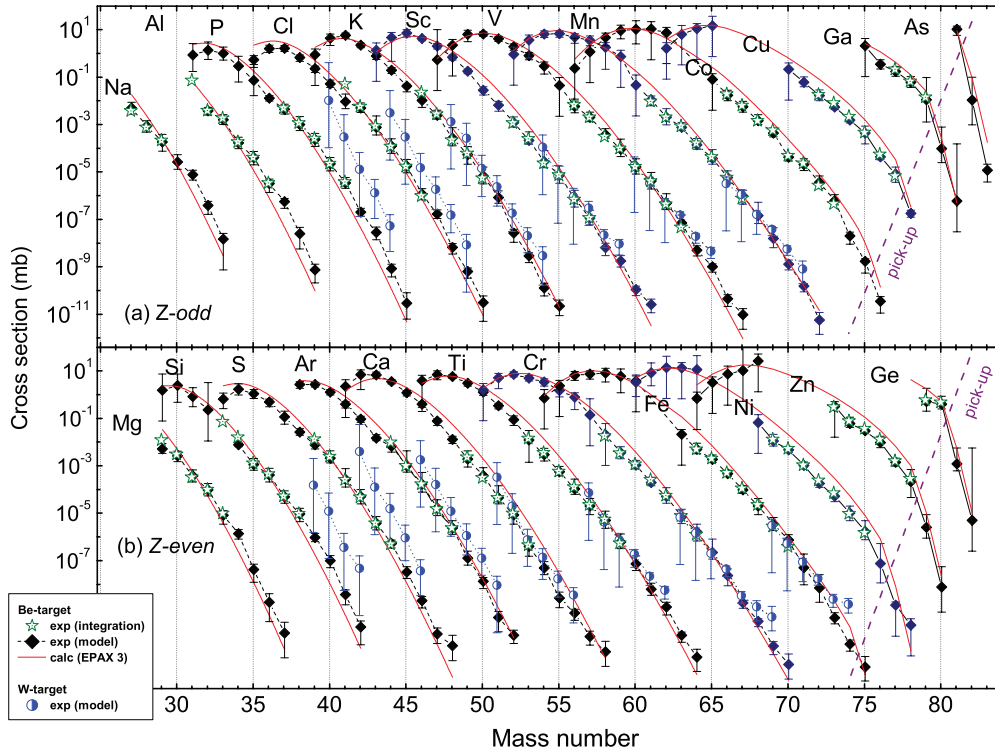


FIG. 6. (Color online) Inclusive production cross sections for fragments from the reaction of  $^{82}\text{Se}$  with beryllium and tungsten targets shown as a function of the mass number. The cross sections with the beryllium targets derived by momentum distribution integration are shown by stars, and those normalized with LISE<sup>++</sup> transmission calculations are indicated by solid diamonds. The cross sections obtained with the tungsten target were normalized with LISE<sup>++</sup> transmission calculations. The red solid lines show the predictions of the EPAX3 systematics [40] for beryllium (see text). The two magenta dashed lines separate nuclei that require neutron pickup in the production mechanism.

separator system. A total of 126 cross sections with beryllium targets were obtained from the Gaussian fits to the longitudinal momentum distributions; these nuclei are indicated by stars in Fig. 6. The cross sections for all of the remaining fragments with incompletely measured longitudinal momentum distributions were obtained with estimated transmission corrections as in our previous work [1]. The parameters for the transmission corrections were assumed to be smoothly varying with  $A$  and  $Z$ .

The cross sections obtained for all the fragments observed in this experiment are shown in Fig. 6 along with the predictions of the recent EPAX3 parametrization [40]. For those isotopes that relied on transmission calculations, the weighted mean of all measured yields was used to obtain the cross section (shown by solid diamonds in Fig. 6). The uncertainties in these cases include the statistical, the systematic, and the transmission correction uncertainties. For more details see Ref. [34]. As can be seen in Fig. 6, the cross sections are in good agreement with those produced by integrating the measured longitudinal momentum distributions in the cases where there is an overlap.

It is important to note that the predictions of the recent EPAX3 parametrization for reactions with beryllium, shown by the solid lines in Fig. 6, reproduce the measured cross sections for isotopes much better than the previous EPAX2.15 predictions [41].

### C. $Q_g$ systematics

The production cross sections for the most neutron-rich projectile fragments have been previously shown to have an exponential dependence on  $Q_g$ , where  $Q_g$  is defined as the difference in mass excess between the beam particle and the observed fragment [2,5]. To test this behavior, the cross sections for each isotopic chain were fitted with the simple expression

$$\sigma(Z, A) = k(Z)\exp[Q_g(Z, A)/T(Z)], \quad (2)$$

where  $T$  represents an inverse slope parameter and  $k$  is a normalization.

Most of the data from the reactions of  $^{82}\text{Se}$  on Be targets in this experiment could be fitted by two inverse slopes with a floating connection point. The trends of the general increase in  $T$  for all of the heavy isotopes of elements  $Z = 19, 20,$  and  $21$  observed with a  $^{76}\text{Ge}$  beam in our previous experiment are reproduced here with the  $^{82}\text{Se}$  beam. The cases of  $Z = 16, 19, 20,$  and  $22$  are illustrated in Fig. 7 showing the measured cross sections versus  $Q_g$  calculated using the masses deduced from the shell model with the GXPFB5 interaction [29]. As in the previous experiment, the heaviest isotopes of elements in the vicinity of  $Z = 20$  appear to deviate from an exponential dependence. The change of slope is most dramatic at  $Z = 20$ . At  $Z = 22$ , the trends show little change in slope for the heaviest isotopes. As was pointed out in our previous study [2],

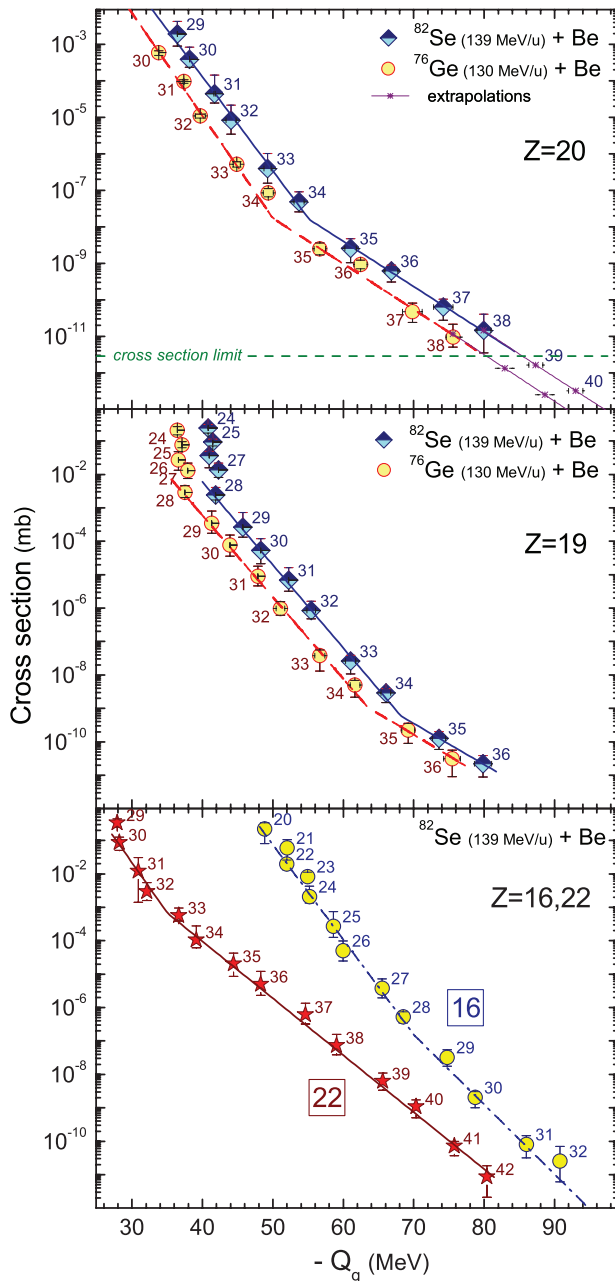


FIG. 7. (Color online) Measured cross sections versus  $-Q_g$  for the production of neutron-rich calcium (top panel) and potassium (middle panel) isotopes from reactions of  $^{82}\text{Se}$  and  $^{76}\text{Ge}$  with a beryllium target. Production cross sections of sulfur and titanium isotopes from the reaction of  $^{82}\text{Se}$  with a beryllium target are shown in the bottom panel. See text for explanation of  $Q_g$  and the lines. Neutron numbers of isotopes are shown in the figure. A horizontal dashed green line in the top panel shows the cross-section limit reached in the experiment with the  $^{82}\text{Se}$  beam.

a possible explanation for the exponential slope reduction at larger masses for these elements is a change in binding energy relative to predictions. It should be noted that the systematic variation of the production cross sections of the calcium isotopes as a function of  $Q_g$  was checked in our previous work with several other well-known mass models

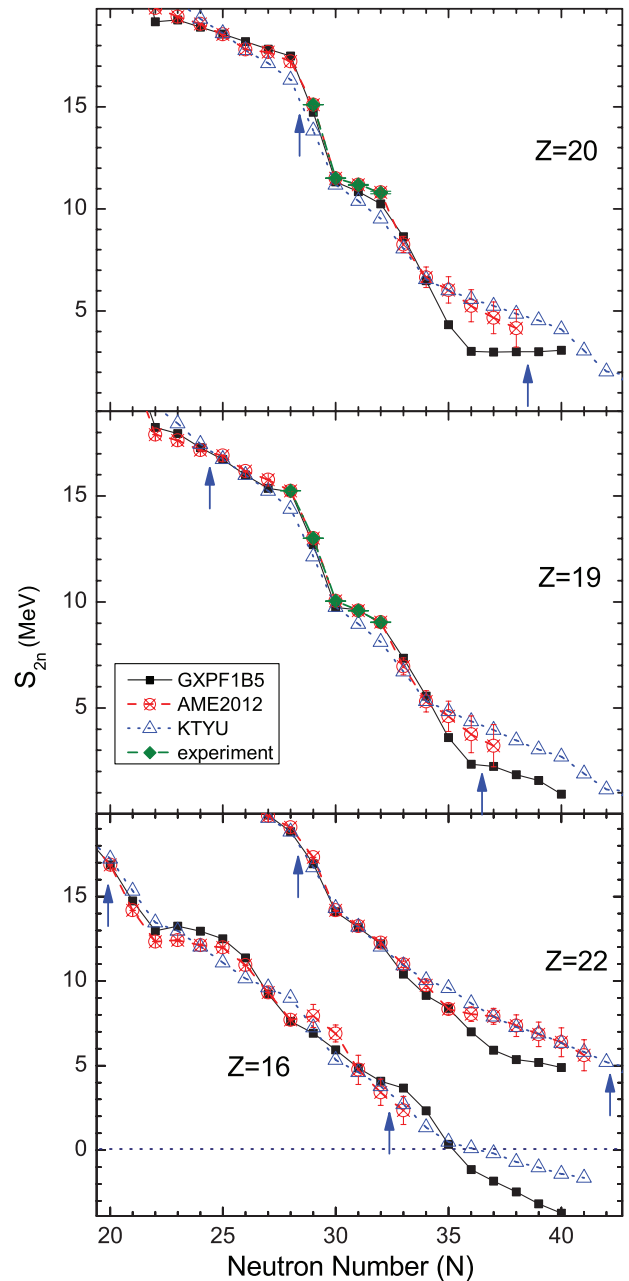


FIG. 8. (Color online) The two-neutron separation energy  $S_{2n}$  deduced from mass values as a function of the neutron number for calcium (top), potassium (middle), and sulfur and titanium isotopes (bottom). Those from experimental mass values [42] are shown by diamonds and those from AME2012 [43] by crossed circles. Results based on the full  $pf$ -shell phenomenological GXPf1B5 [29] interaction and the KTYU mass model [7] are shown by solid squares and empty triangles, respectively. Arrows show regions of isotopes whose measured cross sections are shown in Fig. 7.

and essentially the same behavior was observed (for details, see Fig. 10 in Ref. [1]).

A hint at the origin of the cross-section systematics may be seen in the binding energy trends demonstrated in Fig. 8, where the dependence of  $S_{2n}$  is shown as a function of the neutron number in the neutron-rich region for sulfur,

potassium, calcium, and titanium based on masses from models and experimentally measured values. There is no abrupt behavior for potassium and calcium in the KTYU model [7] or the AME2012 mass table [43]. The slopes of the trends for both elements in the region  $34 \leq N \leq 40$  do not change significantly. On the other hand for two-neutron separation energy lines calculated with the full  $pf$ -shell phenomenological GXPF1B5 [26] interactions, changes in the slope are observed between  $N = 35$  and  $N = 36$  for potassium and calcium isotopes near the same neutron number where the cross-section systematics change. Because  $^{55}\text{Ca}$  ( $N = 35$ ) is predicted by the shell model with the GXPF1B5 effective interaction [29] to have a low one-neutron separation energy of 0.75 MeV, we might expect that the change of slope in Fig. 7 would correspond to  $N = 35$  instead of  $N = 36$ . Thus, it is possible that the trends seen in our cross-section data reflect the  $N = 34$  subshell closure predicted by the GXPF1B5 shell model [29]. Similar breaks in the slopes are seen in the data at  $N = 28$ , but they are not as dramatic as those at  $N = 34$ .

#### D. Global trends of cross sections

A way to visualize the possible effect of the  $N = 34$  subshell closure is to plot the production cross sections versus atomic number. Figure 9 shows the data connected by lines of constant  $N - 2Z$ , which represent changes between nuclei different by a triton, and the label at each point is the neutron number ( $N$ ). This ensemble of lines exhibits a large dip at the shell closure at  $Z = 20$  in the region of  $^{54-56}\text{Ca}$  highlighted

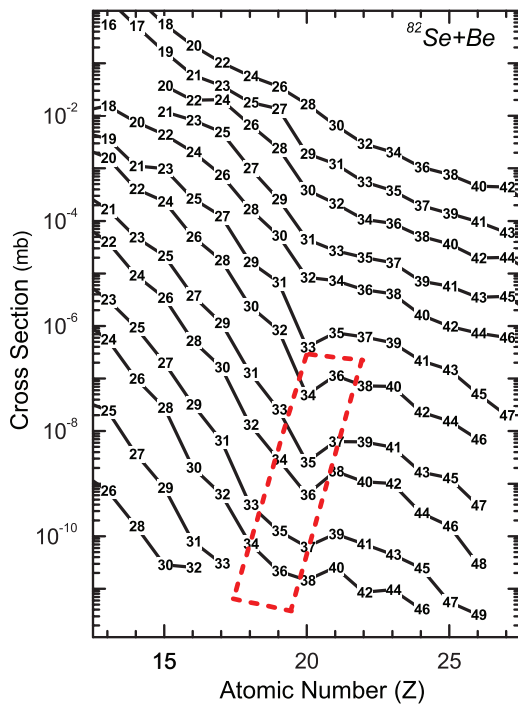


FIG. 9. (Color online) Production cross section versus atomic number ( $Z$ ) for fragments from the reaction of  $^{82}\text{Se}$  with beryllium targets. Lines are connected according to constant  $N - 2Z$ , while labels represent the neutron number. Reactions resulting in neutron pickup are omitted. The red dashed quadrangle is explained in the text.

by the red dashed quadrangle. The same dip can be observed in a similar figure generated from the cross sections measured in the  $^{76}\text{Ge}$  measurements [1].

A reason that these trends may be visible in lines of  $N - 2Z$  in Fig. 9 is that such nuclei have approximately the same neutron separation energy and the drip-line lies close to an  $N - 2Z$  line for  $16 \leq Z \leq 23$ . Further, each line connects nuclei with either an odd or an even number of neutrons; hence, the large odd-even difference in nuclear binding due to pairing is not present along each line. For a constant separation energy we expect the cross section to fall smoothly with  $Z$  in Fig. 9. At  $Z = 20$  and  $N = 34$  the (sub)shell closures correspond to a lower  $S_{1n}$  and  $S_{2n}$  and might be responsible for the dip in the trends, highlighted by the red box.

To illustrate this, two-neutron separation energy  $S_{2n}$  versus neutron number ( $N$ ) of elements  $12 \leq Z \leq 22$  calculated with the full  $pf$ -shell GXPF1B5 interactions [29] is shown in Fig. 10. The label at each point is the atomic number ( $Z$ ) and the red dashed quadrangle encompasses the same region as the one in Fig. 9 for isotopes with  $34 \leq N \leq 37$  and  $18 \leq Z \leq 21$ . The  $N = 34$  subshell closure results in a lowering of the  $S_{2n}$  values for  $Z = 20$  as seen in the figure, corresponding to the same nuclei that have relatively low production cross sections compared to the  $N - 2Z$  trends in Fig. 9.

Based on the observations discussed above, it seems possible that the production-cross-section systematics provide a hint of a change of the nuclear mass surface. The effect is most pronounced close to the drip-line. Plotting the cross

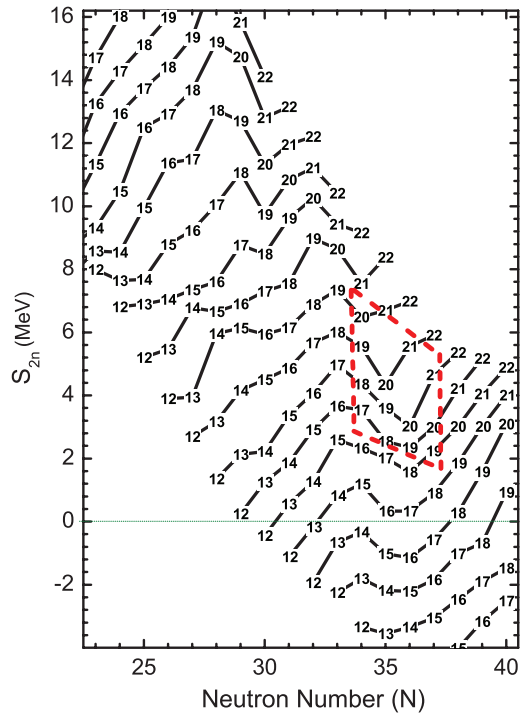


FIG. 10. (Color online) Two-neutron separation energy ( $S_{2n}$ ) versus neutron number ( $N$ ) for elements  $12 \leq Z \leq 22$ . Values are calculated using results from the GXPF1B5 [29] model. Labels in the lines show the atomic numbers of the nuclei. The red dashed quadrangle is explained in the text.

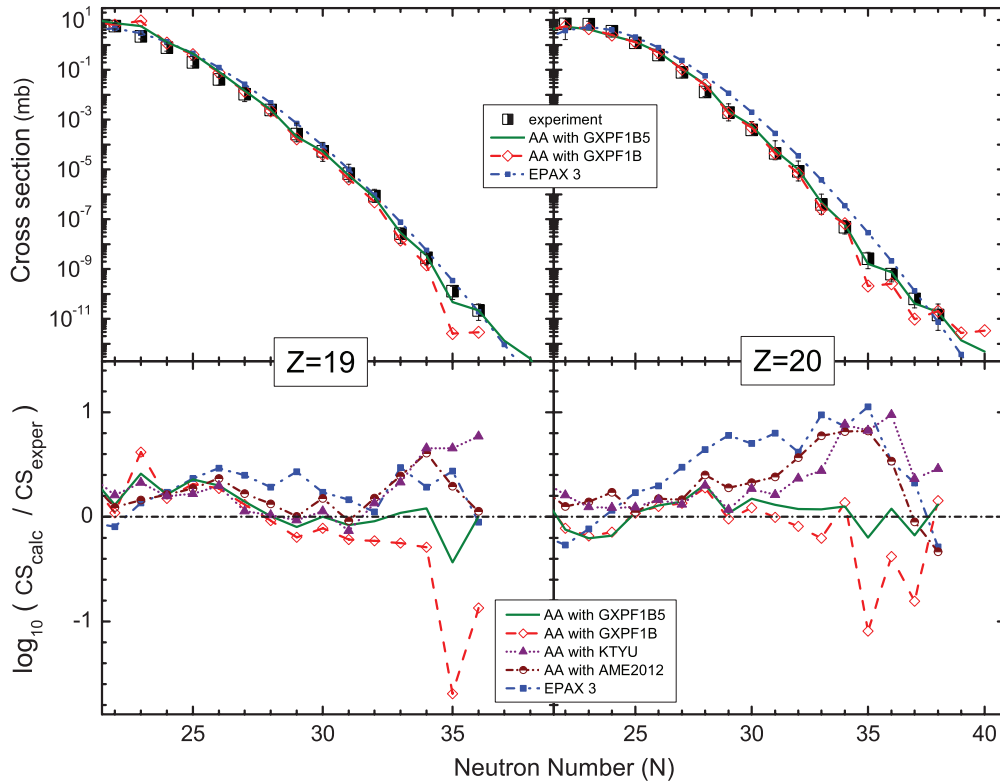


FIG. 11. (Color online) Top: The cross section versus neutron number for the production of neutron-rich potassium (left) and calcium (right) isotopes from the reaction of  $^{82}\text{Se}$  on beryllium targets. The measured values are shown by semisolid rectangles. The results from the abrasion-ablation calculations using the masses obtained via both the GXPFB1B and GXPFB1B5 interactions [29] are shown by open diamonds with dashed lines and solid lines, respectively. For comparison, the values obtained from the EPAX3 systematics [40] (small solid rectangles with dashed-dot-dot lines) are also included. Bottom: Logarithm ratios of calculated and experimental cross sections shown for clearer presentation differences between experimental and calculated values. This presentation includes results from the KTYU model [7] (solid triangles with dotted lines) and the AME2012 table [43] (semisolid circles with dash-dotted lines).

section of elements against  $Q_g$  can exhibit sudden changes in slope that are correlated with regions of changes in the nuclear structure, such as (sub)shell closures.

### E. Abrasion-ablation model

To test the relationship between cross sections and separation energies, the production cross sections obtained in this experiment were compared with those from calculations with the abrasion-ablation model [44] implemented in the LISE++ code [33]. Results for neutron-rich isotopes of potassium and calcium using different mass models are shown in Fig. 11. Predictions of the EPAX3 systematics are shown on the plots for comparison. An excitation energy of 15 MeV per abraded nucleon was deduced from an experimental data fit of the abrasion-ablation (AA) model with AME2012 masses [43] and masses deduced from the shell model using the GXPFB1B interactions [26], whereas a value of 18 MeV has been obtained with KTYU masses [7]. The LISE++ LDM1 parametrization was used to extrapolate masses of very neutron-rich nuclei absent in AME2012 and GXPFB1B mass predictions. The AA model with GXPFB1B masses significantly underestimates cross sections for isotopes with  $N \geq 35$  such as  $^{54,55}\text{K}$  and  $^{55-57}\text{Ca}$ , whereas fair agreement is observed using GXPFB1B

masses. Decreasing the effective energy gap between adjacent neutron single-particle orbitals  $f_{5/2}$  and  $p_{1/2}$  in GXPFB1B makes isotopes with  $36 \leq N \leq 40$  around calcium more particle bound; therefore the result of the  $^{54}\text{Ca}$   $E_x(2_1^+)$  measurement [28] is in good agreement with the measured cross sections and those calculated using the AA model with GXPFB1B5 masses.

On the other hand the mass models that don't predict the slope changes at  $N = 36$  in the  $S_{2n}$  figure (see Fig. 8) overestimate the cross sections for neutron-rich potassium and calcium isotopes (see AA calculations with masses from the KTYU model [7] in Fig. 11).

### F. Estimation of $^{60}\text{Ca}$ production cross section

Based on experimental  $Q_g$  systematics (Fig. 7) and AA model calculations (Fig. 11) using GXPFB1B5 masses, it is possible to estimate the production cross sections for the next unobserved calcium isotopes using a  $^{82}\text{Se}$  beam (See Table II). According to this extrapolation, to observe one event of  $^{59}\text{Ca}$ , the beam intensity has to be increased by a factor of 2 compared to this experiment. For the case of  $^{60}\text{Ca}$ , at least an order magnitude higher beam intensity is needed. It is important to note, that the EPAX3 systematics [40] predict a factor of 20 less

TABLE II. Calculated  $^{59,60}\text{Ca}$  production cross section in  $^{76}\text{Ge} + ^9\text{Be}$  and  $^{82}\text{Se} + ^9\text{Be}$  reactions. Masses calculated with the GXPF1B5 interaction have been used for the  $Q_g$  systematics and the LISE<sup>++</sup> abrasion-ablation model calculations.

Primary beam	Estimation method	$^{59}\text{Ca}$ cross section (mb)	$^{60}\text{Ca}$ cross section (mb)
$^{82}\text{Se}$	AA	1.39e-12	4.83e-13
$^{82}\text{Se}$	$Q_g$	1.62e-12	3.19e-13
$^{76}\text{Ge}$	$Q_g$	1.36e-12	2.47e-13
$^{82}\text{Se}$	EPAX3	3.73e-13	1.65e-14
$^{76}\text{Ge}$	EPAX3	3.68e-13	1.71e-14

production for the  $^{60}\text{Ca}$  isotope, compared to both  $Q_g$  systematics and AA calculations [ $4(\pm 1) \times 10^{-13}$  mb], that makes the search for  $^{60}\text{Ca}$  more likely to be successful in the near future.

## V. SUMMARY

The present study of fragmentation of a  $^{82}\text{Se}$  beam at 139 MeV/u found evidence for four previously unobserved neutron-rich isotopes ( $^{64}\text{Ti}$ ,  $^{67}\text{V}$ ,  $^{69}\text{Cr}$ , and  $^{72}\text{Mn}$ ). The longitudinal momentum distributions and cross sections for a large number of neutron-rich nuclei produced by the  $^{82}\text{Se}$  beam were measured by varying the target thickness in a two-stage fragment separator using a narrow momentum selection. The momentum distributions of 126 neutron-rich isotopes of elements with  $11 \leq Z \leq 32$  were compared to models that describe the shape and centroid of momentum distributions. From these measurements we have obtained a new set of parameters for the semiempirical momentum distribution models [35,36].

The most neutron-rich nuclei of elements with  $Z = 19$  to 21 have been produced with an enhanced rate compared

to the systematics of the production cross sections from the  $Q_g$  systematics. This trend was previously reported for the fragmentation of a  $^{76}\text{Ge}$  beam [2], and therefore the current results confirm those of our previous experiment. This is an indication of a change in the nuclear mass surface near  $Z = 20$  for very neutron-rich nuclei. This result has been explained with a shell model that predicts a subshell closure at  $N = 34$  and a more pronounced one at  $Z = 20$ . We have shown that production-cross-section systematics can provide a hint of a change of the nuclear mass surface close to the drip-line. Plotting the cross section of elements against  $Q_g$  can exhibit sudden changes in slope that are correlated with regions of changes in the nuclear structure, such as (sub)shell closures. A correlation to the nuclear mass models has been shown via plots of the two-neutron separation energy.

It has been shown that the AA model is very sensitive to the input mass values for the most exotic nuclei. The measured cross sections were best reproduced by using masses derived from the full  $pf$  shell-model space with the GXPF1B5 [26] effective interaction modified to a recent  $^{54}\text{Ca}$   $E_x(2_1^+)$  measurement [28].

The cross section for production of  $^{60}\text{Ca}$  using a  $^{82}\text{Se}$  beam on beryllium has been estimated at  $4(\pm 1) \times 10^{-16}$  b. This estimate is based on both  $Q_g$  systematics and AA calculations using masses derived from the shell-model effective interaction GXPF1B5 [29].

## ACKNOWLEDGMENTS

The authors would like to acknowledge the operations staff of the National Superconducting Cyclotron Laboratory for developing the intense  $^{82}\text{Se}$  beam necessary for this study. This work was supported by the US National Science Foundation under Grants No. PHY-06-06007, No. PHY-10-68217, and No. PHY-11-02511. Discussions with Professor V. G. Zelevinsky are very appreciated.

- 
- [1] O. B. Tarasov, M. Portillo, A. M. Amthor, T. Baumann, D. Bazin, A. Gade, T. N. Ginter, M. Hausmann, N. Inabe, T. Kubo, D. J. Morrissey, A. Nettleton, J. Pereira, B. M. Sherrill, A. Stolz, and M. Thoennessen, *Phys. Rev. C* **80**, 034609 (2009).
  - [2] O. B. Tarasov, D. J. Morrissey, A. M. Amthor, T. Baumann, D. Bazin, A. Gade, T. N. Ginter, M. Hausmann, N. Inabe, T. Kubo, A. Nettleton, J. Pereira, M. Portillo, B. M. Sherrill, A. Stolz, and M. Thoennessen, *Phys. Rev. Lett.* **102**, 142501 (2009).
  - [3] T. Ohnishi *et al.*, *J. Phys. Soc. Jpn.* **79**, 073201 (2010).
  - [4] T. Baumann, A. M. Amthor, D. Bazin, B. A. Brown, C. M. Folden III, A. Gade, T. N. Ginter, M. Hausmann, M. Matos, D. J. Morrissey, M. Portillo, A. Schiller, B. M. Sherrill, A. Stolz, O. B. Tarasov, and M. Thoennessen, *Nature (London)* **442**, 1022 (2007).
  - [5] O. B. Tarasov, T. Baumann, A. M. Amthor, D. Bazin, C. M. Folden III, A. Gade, T. N. Ginter, M. Hausmann, M. Matos, D. J. Morrissey, A. Nettleton, M. Portillo, A. Schiller, B. M. Sherrill, A. Stolz, and M. Thoennessen, *Phys. Rev. C* **75**, 064613 (2007).
  - [6] P. F. Mantica, H. L. Crawford, J. Pereira, J. S. Pinter, J. B. Stoker, R. Broda, B. Fornal, R. V. F. Janssens, X. Wang, S. Zhu, N. Hoteling, W. B. Walters, C. R. Hoffman, and S. L. Tabor, *Bull. Am. Phys. Soc.* **53**, 64 (2008).
  - [7] H. Koura, T. Tachibana, M. Uno, and M. Yamada, *Prog. Theor. Phys.* **113**, 305 (2005).
  - [8] C. Thibault, R. Klapisch, C. Rigaud, A. M. Poskanzer, R. Prieels, L. Lessard, and W. Reisdorf, *Phys. Rev. C* **75**, 644 (1975).
  - [9] X. Campi, H. Flocard, A. K. Kerman, and S. Koonin, *Nucl. Phys. A* **251**, 193 (1975).
  - [10] E. K. Warburton, J. A. Becker, and B. A. Brown, *Phys. Rev. C* **41**, 1147 (1990).
  - [11] D. Guillemaud-Mueller, C. Detraz, M. Langevin, F. Naulin, M. D. Saint-Simon, C. Thibault, F. Touchard, and M. Epherre, *Nucl. Phys. A* **426**, 37 (1984).
  - [12] T. Motobayashi, Y. Ikeda, Y. Ando, K. Ieki, M. Inoue, N. Iwasa, T. Kikuchi, M. Kurokawa, S. Moriya, S. Ogawa, H. Murakami, S. Shimoura, Y. Yanagisawa, T. Nakamura, Y. Watanabe, M. Ishihara, T. Teranishi, H. Okuno, and R. F. Casten, *Phys. Lett. B* **346**, 9 (1995).

- [13] K. Yoneda *et al.*, *Phys. Lett. B* **499**, 233 (2001).
- [14] Y. Yanagisawa *et al.*, *Phys. Lett. B* **566**, 84 (2003).
- [15] J. A. Church, C. M. Campbell, D.-C. Dinca, J. Enders, A. Gade, T. Glasmacher, Z. Hu, R. V. F. Janssens, W. F. Mueller, H. Olliver, B. C. Perry, L. A. Riley, and K. L. Yurkewicz, *Phys. Rev. C* **72**, 054320 (2005).
- [16] M. Hannawald, T. Kautzsch, A. Wöhr, W. B. Walters, K.-L. Kratz, V. N. Fedoseyev, V. I. Mishin, W. Bohmer, B. Pfeiffer, V. Sebastian, Y. Jading, U. Koster, J. Lettry, H. L. Ravn, and the ISOLDE Collaboration, *Phys. Rev. Lett.* **82**, 1391 (1999).
- [17] O. Sorlin *et al.*, *Eur. Phys. J. A* **16**, 55 (2003).
- [18] P. Adrich, A. M. Amthor, D. Bazin, M. D. Bowen, B. A. Brown, C. M. Campbell, J. M. Cook, A. Gade, D. Galaviz, T. Glasmacher, S. McDaniel, D. Miller, A. Obertelli, Y. Shimbara, K. P. Siwek, J. A. Tostevin, and D. Weisshaar, *Phys. Rev. C* **77**, 054306 (2008).
- [19] N. Aoi *et al.*, *Phys. Rev. Lett.* **102**, 012502 (2009).
- [20] A. Gade *et al.*, *Phys. Rev. C* **81**, 051304 (2010).
- [21] W. Rother *et al.*, *Phys. Rev. Lett.* **106**, 022502 (2011).
- [22] S. Zhu *et al.*, *Phys. Rev. C* **74**, 064315 (2006).
- [23] B. A. Brown, *Prog. Part. Nucl. Phys.* **47**, 517 (2001).
- [24] S. M. Lenzi, F. Nowacki, A. Poves, and K. Sieja, *Phys. Rev. C* **82**, 054301 (2010).
- [25] P. F. Mantica, R. Broda, H. L. Crawford, A. Damaske, B. Fornal, A. A. Hecht, C. Hoffman, M. Horoi, N. Hoteling, R. V. F. Janssens, J. Pereira, J. S. Pinter, J. B. Stoker, S. L. Tabor, T. Sumikama, W. B. Walters, X. Wang, and S. Zhu, *Phys. Rev. C* **77**, 014313 (2008).
- [26] M. Honma, T. Otsuka, B. A. Brown, and T. Mizusaki, *Eur. Phys. J. A* **25**, Suppl. 1, 499 (2005).
- [27] A. Poves, J. Sánchez-Solano, E. Caurier, and F. Nowacki, *Nucl. Phys. A* **694**, 157 (2001).
- [28] D. Steppenbeck, talk given at the International Symposium “Exotic Nuclear Structure From Nucleons” (ENSNF 2012), Tokyo, Japan, October 10–12, 2012.
- [29] Y. Utsuno, T. Otsuka, B. A. Brown, M. Honma, T. Mizusaki, and N. Shimizu, *Phys. Rev. C* **86**, 051301(R) (2012).
- [30] D. J. Morrissey, B. M. Sherrill, M. Steiner, A. Stolz, and I. Wiedenhöver, *Nucl. Instrum. Methods Phys. Res., Sect. B* **204**, 90 (2003).
- [31] D. Bazin, J. Caggiano, B. M. Sherrill, J. Yurkon, and A. Zeller, *Nucl. Instrum. Methods Phys. Res., Sect. B* **204**, 629 (2003).
- [32] R. Grzywacz *et al.*, *Phys. Lett. B* **355**, 439 (1995).
- [33] O. B. Tarasov and D. Bazin, *Nucl. Instrum. Methods Phys. Res., Sect. B* **266**, 4657 (2008), <http://lise.nslc.msu.edu>.
- [34] O. B. Tarasov, D. Bazin, T. Baumann, A. Gade, T. N. Ginter, M. Hausmann, D. J. Morrissey, J. Pereira, M. Portillo, B. M. Sherrill, A. Stolz, and M. Thoennessen, *Nucl. Instrum. Methods Phys. Res., Sect. A* **620**, 578 (2010).
- [35] A. S. Goldhaber, *Phys. Lett. B* **53**, 306 (1974).
- [36] D. J. Morrissey, *Phys. Rev. C* **39**, 460 (1989).
- [37] O. B. Tarasov *et al.* (unpublished).
- [38] O. Tarasov, *Nucl. Phys. A* **734**, 536 (2004).
- [39] V. Borrel, D. Guerreau, J. Galin, B. Gatty, D. Jacquet, and X. Tarrago, *Z. Phys. A* **314**, 191 (1983).
- [40] K. Sümmerer, *Phys. Rev. C* **86**, 014601 (2012).
- [41] K. Sümmerer and B. Blank, *Phys. Rev. C* **61**, 034607 (2000).
- [42] A. T. Gallant *et al.*, *Phys. Rev. Lett.* **109**, 032506 (2012).
- [43] M. Wang, G. Audi, A. H. Wapstra, F. G. Kondev, M. MacCormick, X. Xu, and B. Pfeiffer, *Chin. Phys. C* **36**, 1603 (2012).
- [44] O. B. Tarasov and D. Bazin, *Nucl. Instrum. Methods Phys. Res., Sect. B* **207**, 174 (2003).